Lawrence Berkeley National Laboratory
LBL Publications

Title
Optimizing Vertical Crystallization for Efficient Perovskite Solar Cells by Buried Composite Layers

Permalink
https://escholarship.org/uc/item/2f17c6m9

Journal
Solar RRL, 5(10)

ISSN
2367-198X

Authors
Yang, Xiaoyu
Li, Lei
Wu, Jiang
et al.

Publication Date
2021-10-01

DOI
10.1002/solr.202100457

Peer reviewed

Optimizing Vertical Crystallization for Efficient Perovskite Solar Cells by Buried Composite Layers

Xiaoyu Yang,* Lei Li, Jiang Wu, Qin Hu, Yanju Wang, Thomas P. Russell, Yongguang Tu,* and Rui Zhu

Planar-heterojunction perovskite solar cells (PSCs) have experienced rapid evolution in recent years because of the low-temperature processing, suitable alignment, and high mobility of the tin oxide buried contact layer. However, improper SnO_2 surface states and poor crystallinity of the top perovskite films are still the main obstacles for the planar PSCs in which performance always lags behind their mesoporous counterparts. Herein, a new buried contact is reported by introducing graphitic carbon nitride (g-C_3N_4) into the commonly used SnO_2 which performs outstanding transmittance, conductivity, and surface states for a high-quality electron-transporting layer. Moreover, the vertical composition and crystallinity of the top perovskite film are manipulated by rich amino groups on the edge of the g-C_3N_4 nanosheets which induce the prenucleation of the lead-rich species at the buried interface. Benefiting from the high-quality buried contacts and the optimized perovskite layers, the resultant PSCs achieve a champion efficiency of 21.5% with all photovoltaic parameters enhanced in comparison with their control counterparts ($<$20%).

1. Introduction

Perovskite solar cell (PSC) has witnessed rapid progress over the past 10 years, which makes it the most promising photovoltaic technology.[1–8] Metal oxide buried contact layers (BCLs), such as the titanium oxide (TiO_2) and tin oxide (SnO_2), have promoted the development of PSCs due to their interfacial compatibility, superior transmittance, and good reproducibility.[9,10] In comparison with the mesoporous TiO_2 BCLs, the planar SnO_2 BCLs have attracted enormous attention because of their low-temperature fabrication, high electron mobility, and suitable band alignment with the commonly used transparent conductive substrates.[11,12] These huge potentials of the SnO_2 BCL accelerate the development of the planar-heterojunction solar cells that have approached the world-record PSC efficiency.[13–15]

Despite the great achievements on efficient perovskite devices, the planar SnO_2 BCL still encounters some drawbacks to realize high-quality top perovskite films. The ultrathin and smooth SnO_2 BCL generally leads to rapid volatilization of the perovskite precursor upon annealing, resulting in the nonideal nucleation and growth of perovskite crystallites in the absence of mesoporous scaffolds.[16–18] Moreover, the improper surface states of the SnO_2 BCL deposited from the colloidal precursor also generate trap/surface states at the buried interface of the perovskite film.[19,20] In brief, the unsatisfied film quality of the perovskite could be one of the main obstacles for the SnO_2-based devices compared with their TiO_2 counterparts. Therefore, the development of the high-quality SnO_2 buried layer for optimizing perovskite

X. Yang, L. Li, J. Wu, Y. Wang, R. Zhu
State Key Laboratory for Artificial Microstructure and Mesoscopic Physics
School of Physics
Frontiers Science Center for Nano-optoelectronics and Collaborative
Innovation Center of Quantum Matter
Peking University
Beijing 100871, China
E-mail: yangxy_seed@pku.edu.cn

J. Wu, R. Zhu
Yangtze Delta Institute of Optoelectronics
Peking University
Nantong, Jiangsu 226010, China

Q. Hu
School of Microelectronics
University of Science and Technology of China
Hefei, Anhui 230026, China

The ORCID identification number(s) for the author(s) of this article can be found under https://doi.org/10.1002/solr.202100457.

T. P. Russell
Department of Polymer Science and Engineering
University of Massachusetts
Amherst, MA 01003, USA

T. P. Russell
Materials Sciences Division
Lawrence Berkeley National Laboratory
Berkeley, CA 94720, USA

Y. Tu
Frontiers Science Center for Flexible Electronics
Xi'an Institute of Flexible Electronics (IFE) and Xi'an Institute of
Biomedical Materials & Engineering
Northwestern Polytechnical University
Xi'an, Shaanxi 710072, China
E-mail: iamygtu@nwpu.edu.cn

R. Zhu
Collaborative Innovation Center of Extreme Optics
Shanxi University
Taiyuan, Shanxi 030006, China

crystallization and realizing outstanding device performances is urgently demanded.

Recently, graphitic carbon nitride (g-C$_3$N$_4$) as a stable n-type semiconductor has shown great potential in the development of the PSCs because of its outstanding chemical properties and good compatibility with halide perovskites.[21] Introducing C$_3$N$_4$-related nanomaterials into the bulk or at the interface of the perovskite active layer could passivate the trap states and enhance the crystallization of the polycrystalline film,[22–26] but developing a facile strategy for collectively optimizing contact and photoactive layers based on the g-C$_3$N$_4$ remains challenging and the exact regulating mechanism of the g-C$_3$N$_4$ on the perovskite is still vague. In this work, we report a new composite BCL (SnO$_2$:g-CN) by introducing graphitic carbon nitride (g-C$_3$N$_4$) nanosheets (50–150 nm; **Figure 1**a) into the SnO$_2$ layer. The SnO$_2$:g-CN BCLs exhibit superior transmittance, conductivity, and surface states for efficient electron extraction at the buried interface. More importantly, the introduced g-C$_3$N$_4$ manipulates the growth of the perovskite film by virtue of its nanosheet template and rich amino groups on the edge, which optimize the vertical composition and crystallization of the polycrystalline perovskite film from the buried interface to the top surface. Residual lead-halide crystallites in the films are rationally controlled and the grain boundaries are reduced, collectively resulting in enhanced charge-carrier lifetimes. In brief, based on the SnO$_2$:g-CN BCL, all photovoltaic parameters were enhanced in the planar PSCs and a champion efficiency of 21.5% was achieved.

2. Results and Discussion

We first evaluated the properties of the newly developed SnO$_2$:g-CN BCL. In Figure 1b, the dark g-C$_3$N$_4$ nanosheets distribute uniformly into the SnO$_2$ layer by simply spin-coating the SnO$_2$:g-CN precursor onto the indium tin oxide (ITO) glass, and the thickness of SnO$_2$:g-CN BCL was measured as about 40 nm. A small amount of C and N could be detected from the X-ray energy dispersive spectrum (EDS) of the SnO$_2$:g-CN/ITO glass (Figure 1c). And N 1s X-ray photoelectron spectroscopy (XPS) spectrum confirms the C—N ($\approx$402.5 eV) and C=N ($\approx$398.8 eV) characteristic signals which attribute to the g-C$_3$N$_4$ nanosheet instead of organic contaminants.[27,28]

The surface chemical states of the SnO$_2$ and SnO$_2$:g-CN BCLs were compared by analyzing the O 1s spectra (Figure 1d). Two characteristic peaks belonging to O^{2-} (at $\approx$530.7 eV) and OH$^-$ (at $\approx$531.9 eV) terminal groups on the SnO$_2$ surface were performed in O 1s spectra, and the OH$^-$ terminals were likely to generate trap states near the valence band of the SnO$_2$ layer.[19,29] With the aid of the introduced acidic g-C$_3$N$_4$ dispersion, we found the peak area of the OH$^-$ terminal group was significantly reduced, which means the eliminated trap states at the SnO$_2$ surface. The increased Fermi level of the SnO$_2$:g-CN further confirmed the variation of the surface chemical termination and indicated a more n-type buried contact layer (Figure S1, Supporting Information), facilitating the extraction of the electrons at the buried interface. However, we cannot identify the diffraction
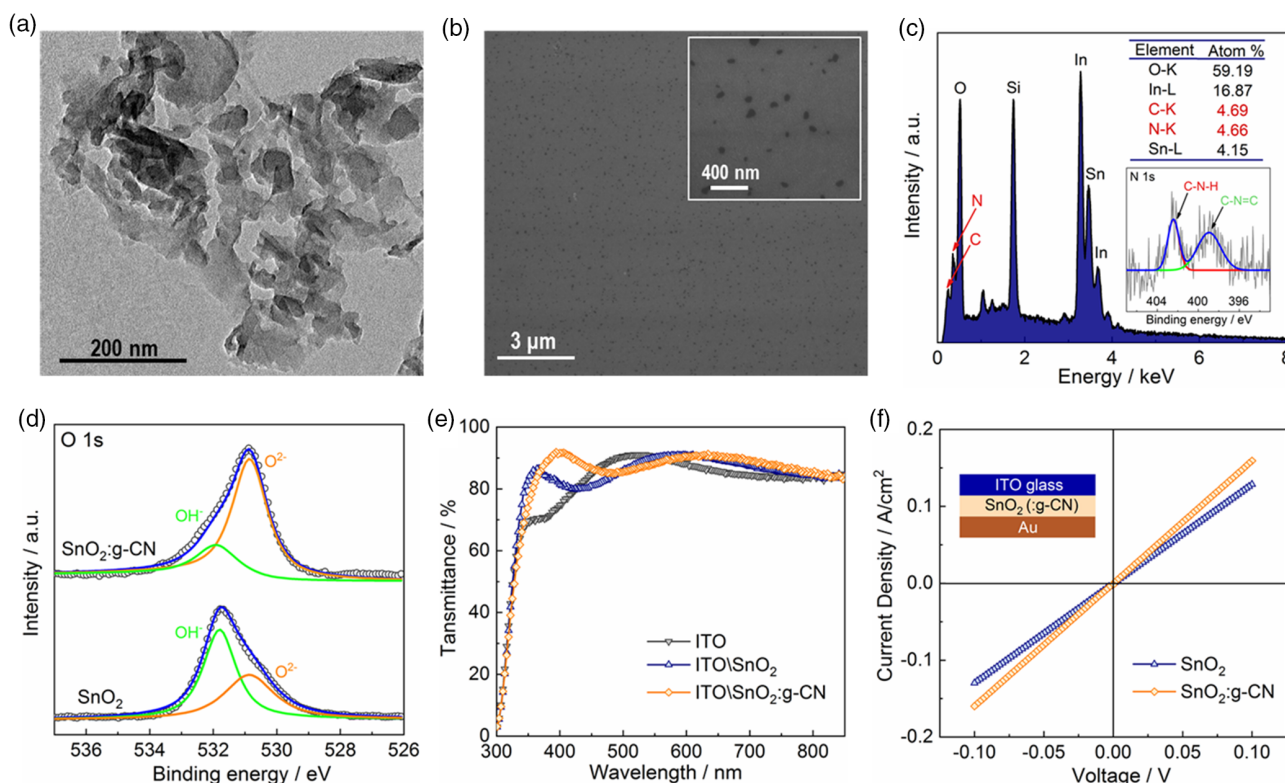

Figure 1. a) Transmission electron microscopy image of the g-C$_3$N$_4$ nanosheet. b) SEM images and c) EDS analysis for the SnO$_2$:g-CN BCL. The inset is the N 1s characteristic spectrum of the SnO$_2$:g-CN. d) O 1s spectra of the SnO$_2$ and SnO$_2$:g-CN BCLs. e) UV–vis transmission spectra for the ITO glass, ITO/SnO$_2$, and ITO/SnO$_2$:g-CN. f) Electrical conductivity measurements for the SnO$_2$ and SnO$_2$:g-CN BCLs.

peaks of SnO_2 or $g-C_3N_4$ for both BCLs because of the weak diffraction signals from the ultrathin BCLs (Figure S2, Supporting Information). From the UV–vis spectra (Figure 1e), the obviously improved transmittance was found in the SnO_2:g-CN BCL compared with the SnO_2 BCL in the range of 350–500 nm. We speculate that the enhanced transmittance derives from the adjustment of incident lights by the evenly distributed $g-C_3N_4$ nanostructures or the possible optical coupling in the SnO_2:g-CN layer.[30–32] Furthermore, we measured the electrical conductivity of the BCLs, which is critical for electron transport at the buried interface (Figure 1f). The direct current conductivity (σ_0) is extracted from the equation, $J = \sigma_0 A d^{-1} V$, where d is the thickness of the BCL and A is the active area. The SnO_2:g-CN BCL (6.2×10^{-5} S cm^{-1}) performs higher conductivity than the SnO_2 BCL (5.0×10^{-5} S cm^{-1}), benefiting from the increased pathways for electron transportation.

To systematically study the film qualities of the perovskites growing onto the SnO_2:g-CN, we performed scanning electron microscopy (SEM) combined with X-ray diffraction (XRD) for surface morphologies and crystallographic information, respectively. In view of that excess PbI_2 in the perovskite film is beneficial for improving the film qualities, we prepared the perovskite precursor with the nonstoichiometric composition of $FA_{0.85}MA_{0.11}Cs_{0.04}PbI_{2.67}Br_{0.33}\cdot xPbI_2$ ($x = 0\%$, 2%, 4%, 6%, and 8%) to fabricate polycrystalline films via one-step antisolvent methods.[7,33] With the increment of introduced PbI_2, the amount of the bright crystallites increases at grain boundaries as shown in **Figure 2**a and Figure S3, Supporting Information, which have been proved to be the lead halides (PbX_2, X = I, Br) in the literature.[3] And the increased PbX_2 peak intensities in the corresponding XRD patterns show consistent results with the SEM images (Figure 2c). Interestingly, for the perovskite films fabricated on the SnO_2:g-CN BCLs, we cannot find any bright PbX_2 crystallites in perovskites from top-view SEM images and corresponding XRD patterns when the introduced PbI_2 less than 4% (Figure 2b,d). Although the excess PbX_2 begins to be detected when the introduced PbI_2 up to 6%, the bright crystallites in the SnO_2:g-CN sample are still less than their SnO_2 counterpart. We also find that the perovskite grain sizes have slight changes with different contents of excess PbX_2. Therefore, we extracted the full width at half maxima (FWHM) of the (110) peaks, belonging to the α-phase perovskites, to estimate the perovskite crystal sizes (Figure 2e). For the SnO_2-based perovskites, the FWHMs seem to have a positive correlation with the peak intensity of PbX_2, indicating excess PbI_2 could cause a smaller crystal grain of the perovskite film.
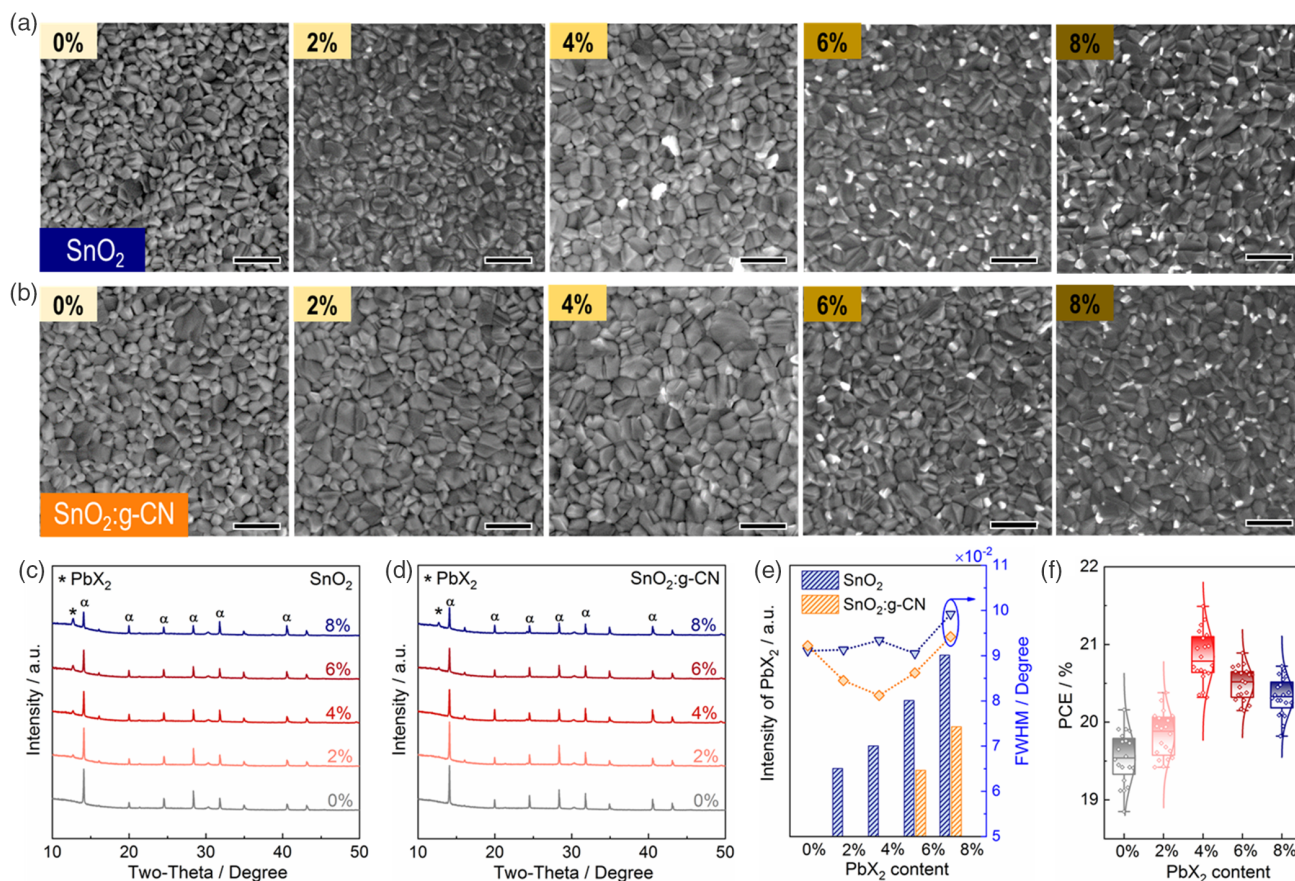

Figure 2. a,b) Surface morphologies of the perovskite films with excess PbI2 contents (0%, 2%, 4%, 6%, and 8%) in precursors grown on the a) SnO_2 and b) SnO_2:g-CN BCLs. Scale bar, 500 nm. c,d) XRD patterns of the perovskite films with excess PbI_2 contents in precursors grown on the c) SnO_2 and d) SnO_2:g-CN BCLs. e) The peak intensities of the PbX_2 and the FWHMs of the α-phase perovskite (110) peaks extracted from (b,c). f) The PCE distributions of the PSCs based on SnO_2:g-CN BCLs with excess PbI_2 contents.

However, SnO$_2$:g-CN-based perovskite films present reduced FWHMs of the perovskite films with the increment of introduced PbI$_2$ from 0% to 4% even though no PbX$_2$ crystallites performed at the film surface. The smallest FWHM means the largest perovskite grains, and therefore, the 4%-excess-PbI$_2$ perovskite based on SnO$_2$:g-CN exhibits the best film quality. To validate the improved film quality by the SnO$_2$:g-CN BCL, we further fabricated planar-heterojunction PSCs comprising indium tin oxide (ITO)/SnO$_2$:g-CN/perovskite/2,2′,7,7′-tetrakis(N,N-dipmethoxy-phenylamine)-9,9′-spirobifluorene (Spiro-OMeTAD)/Au. The statistical distributions of the power conversion efficiencies (PCEs) are shown in Figure 2f and have a tendency consistent with the perovskite quality as demonstrated earlier. The 4%-excess-PbI$_2$ devices perform the best performance, confirming the superior film quality achieved by moderate amounts of excess PbI$_2$ in the precursor growing on the SnO$_2$:g-CN BCL.

To clarify the unique growth of the perovskite film onto the SnO$_2$:g-CN BCL, we performed cross-sectional SEM images of the full devices based on the SnO$_2$ and SnO$_2$:g-CN BCLs (**Figure 3**a,b). For the SnO$_2$:g-CN sample, large perovskite grains are vertically arranged from the buried to top contact layers. In comparison, the SnO$_2$-based perovskite film is composed of many stacked small grains, which confirms the different growth conditions for the perovskites on these two BCLs. The wettability of the buried contact is proved to change the nucleation and growth of the perovskite film, affecting the film quality and the grain size.[34] We thus performed the wettability test for the SnO$_2$, SnO$_2$:g-CN, and g-C$_3$N$_4$, as shown in Figure 3c. We found the slightly worse wettability of the SnO$_2$:g-CN layer (24.4°) than its SnO$_2$ counterpart (23.5°), which benefits from the hydrophobic nature of g-C$_3$N$_4$ (52.9°) to perovskite precursor, probably leading to the dispersed nucleation and growth for achieving larger perovskite grains.

We further evaluated the vertically compositional distributions of the perovskite layers fabricated on different BCLs. As shown in Figure 3d, the ratios of lead (Pb) to halide (X) were calculated
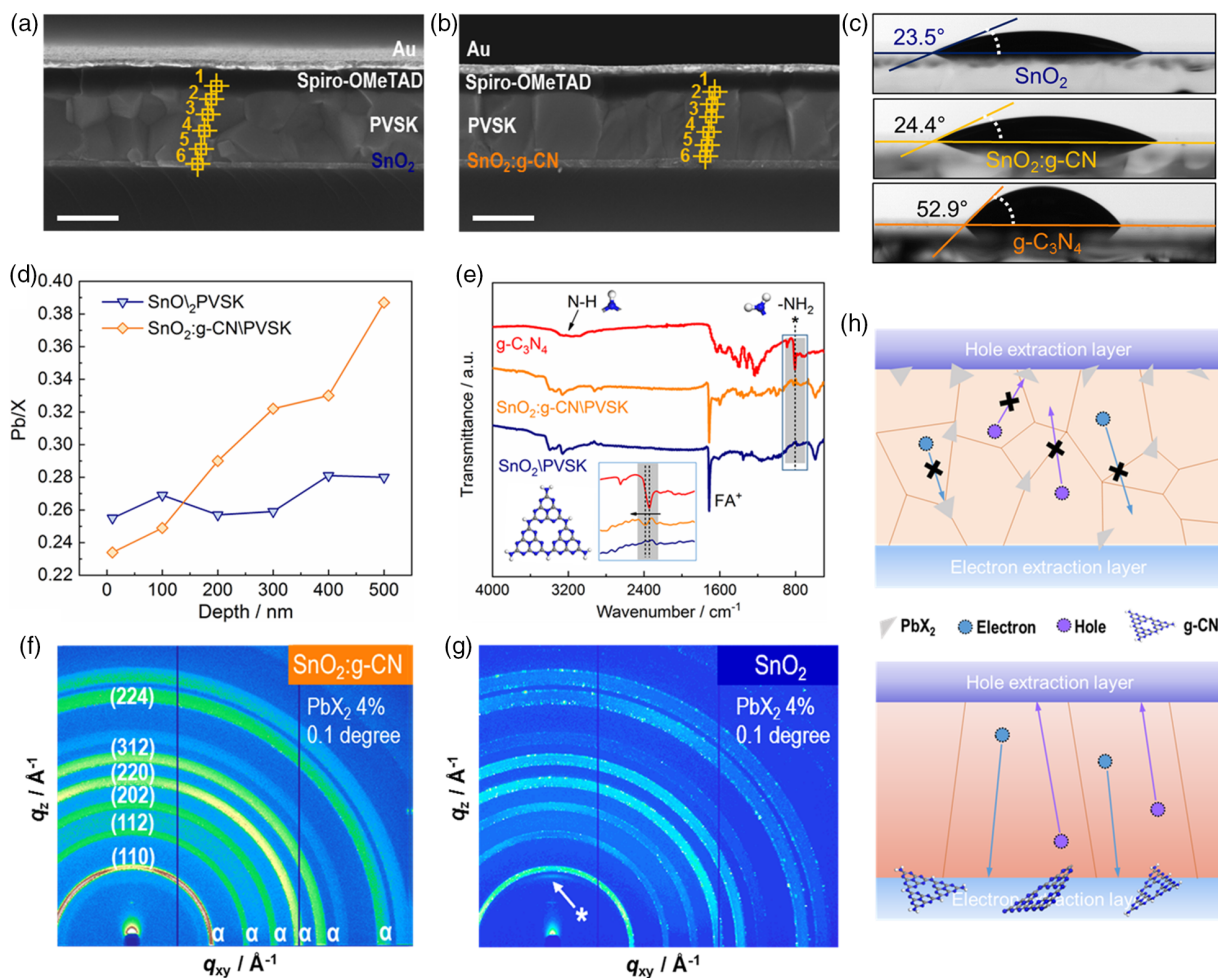

Figure 3. a,b) Cross-sectional SEM images of the planar-heterojunction PSCs based on a) SnO$_2$ and b) SnO$_2$:g-CN BCLs. Scale bar, 500 nm. c) Wettability measurements for the SnO$_2$, SnO$_2$:g-CN, and g-C$_3$N$_4$. The testing solution was the perovskite precursor used for fabricating the perovskite active layer in solar cells. d) Atomic Pb/X ratios at various depths of the perovskite films based on the SnO$_2$ (SnO$_2$\PVSK) and SnO$_2$:g-CN (SnO$_2$:g-CN\PVSK). PVSK: perovskite. e) FTIR spectrum of the g-C$_3$N$_4$ nanosheet, SnO$_2$:g-CN\PVSK, and SnO$_2$\PVSK. f,g) GIWAXS 2D patterns for the perovskite films fabricated on the f) SnO$_2$:g-CN and g) SnO$_2$ BCLs at the beam incidence angle of 0.1°. α and * represent the α-phase perovskites and PbX$_2$, respectively. h) Schematic of the vertical carrier transportation of the perovskite films via buried manipulation.

from the cross-sectional EDS measurement on various depths of the perovskite films (Figure 3a,b and S4, Supporting Information). The Pb/X ratio of the SnO_2-based perovskite film shows a slight variation in the range of 0.25–0.28 at different depths (Figure 3d and S5, Supporting Information). However, for the perovskite film grown on the SnO_2:g-CN, the Pb/X ratio has an obvious positive tendency, increasing from 0.23 to 0.39 with the detecting depths. Therefore, Pb-rich species tend to accumulate at the buried interface during the film growth, which could be the main place for the disappeared PbX_2 known as the Pb-rich component (Pb/X ratio = 0.5) in the perovskite film. Fourier transform infrared (FTIR) spectroscopy confirms the existence of the primary amine (—NH_2) and secondary amine (=N—H) groups in the g-C_3N_4 nanosheet that could coordinate with Pb-related components in the precursor, promoting the pre-nucleation of the Pb-related intermediates onto the SnO_2:g-CN BCLs (Figure 3e). The redshifted infrared signal of —NH_2 (+9 cm^{-1}) in the SnO_2:g-CN/perovskite stack indicates the electron–donor effects of g-C_3N_4 relative to the perovskite films, confirming the chemical interactions between the g-C_3N_4 and the perovskites. Therefore, rich amine groups in the g-C_3N_4 nanosheet have the ability to induce the Pb-rich species first nucleate at the SnO_2:g-CN BCL, manipulating the vertical composition and crystallization of the perovskite film.[5,35–37]

To examine the vertical manipulating effect from the bottom to the top, we further performed the grazing-incidence wide-angle X-ray scattering (GIWAXS) technique to probe the top-surface crystallographic information of the perovskite films with an incidence angle of 0.1°.[33] All the α-phase perovskite signals could be identified on the scattering patterns, as shown in Figure 3f,g. For the SnO_2:g-CN sample, there is no PbX_2 signal but enhanced α-phase signals in comparison with their SnO_2 counterpart, proving the improved surface crystallization of the perovskite film from the buried SnO_2:g-CN contact, which is consistent with the surface morphologies from the SEM results. We draw a schematic for the buried manipulation of the perovskite film in Figure 3h. On the SnO_2 BCL, the poor crystallization of the perovskites combined with abundant grain boundaries and the residual PbX_2 crystallites would inhibit the carrier transportation and even annihilate photogenerated charge carriers. However with the help of the SnO_2:g-CN BCL, the vertical crystallization of the perovskite film is efficiently optimized and the excess PbX_2 is eliminated, promoting the vertical transportation of charge carriers to both contacts.

To validate our findings by the photovoltaic performance, we first screened out the best g-C_3N_4 concentration of the buried composite layer by investigating the electrical properties and the optical properties of the corresponding top perovskite films (Figure S6, Supporting Information). Based on the best choice, the current density–voltage (J–V) curves of the champion planar-heterojunction PSCs are shown in **Figure 4**a. The SnO_2:g-CN device realizes an enhanced open-circuit voltage (V_{OC}) of 1.19 V, a fill factor (FF) of 0.78, a slightly increased short-circuit current density (J_{SC}) of 23.21 mA cm^{-2}, and a champion PCE of
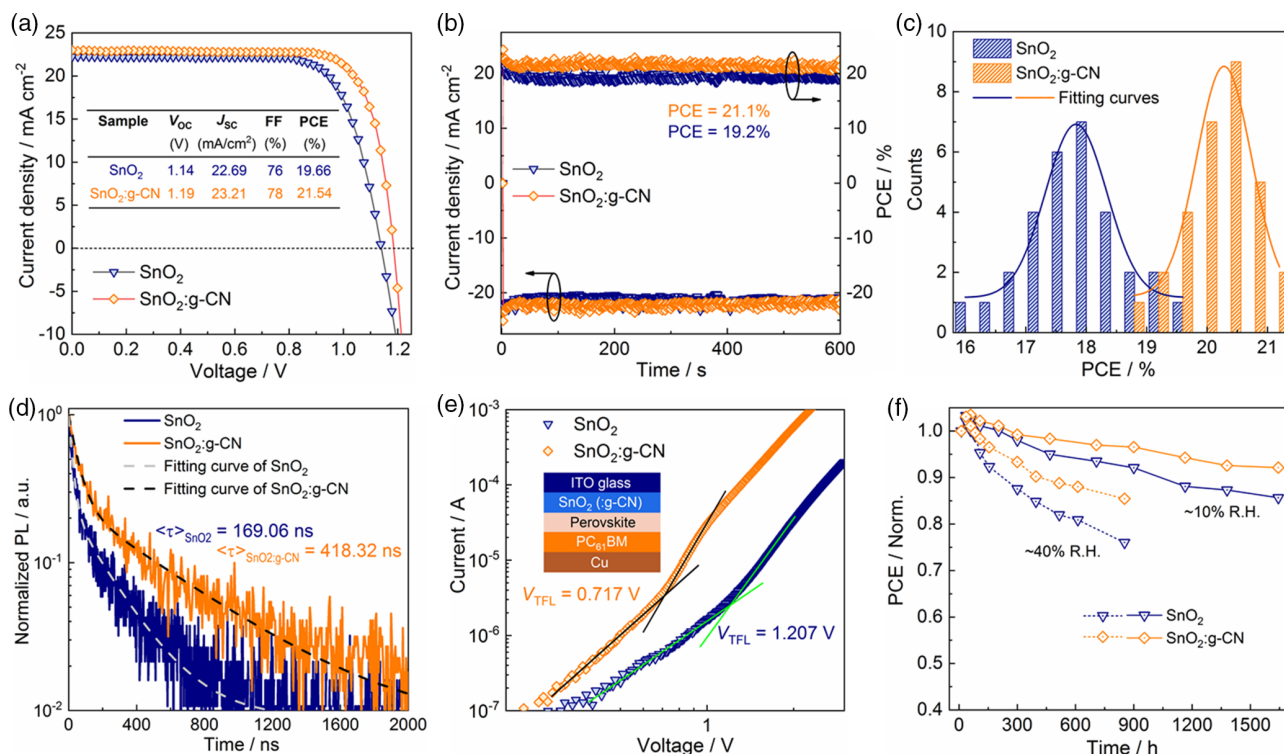

Figure 4. a) J–V curves and corresponding photovoltaic parameters of the champion devices based on the SnO_2 and SnO_2:g-CN BCLs at the reverse scan. b) SPOs and corresponding steady current density outputs for the SnO_2 and SnO_2:g-CN devices. c) Statistical distribution of the PCEs. d) TRPL spectra of perovskite film fabricated on the SnO_2 and SnO_2:g-CN BCLs. e) Electron-only devices for the quantitative measurement of the trap-state density. f) Evolution of the device stabilities for the SnO_2 and SnO_2:g-CN devices stored in ambient conditions at the relative humidity (RH) of ≈10% and ≈40%.

21.54% without any posttreatment in comparison with the control device (a V_{OC} of 1.14 V, a FF of 0.78, a J_{SC} of 22.69 mA cm^{-2}, and a PCE of 19.66%). The enhanced V_{OC} and FF could derive from the improved crystallinity and reduced trap states of the perovskite film, and the increased J_{SC} may benefit from improved photon transmission of the SnO$_2$:g-CN BCL, which is further confirmed by external quantum efficiencies (EQEs) and corresponding integrated current densities (Figure S7, Supporting Information). Moreover, the stabilized power outputs (SPOs) of the SnO$_2$ and SnO$_2$:g-CN devices are 19.2% and 21.1%, respectively, and both devices show negligible hysteresis (Figure 4b and Figure S8, Supporting Information). Statistical results of the device performance are provided as the histogram chart in Figure 4c, confirming a better average efficiency of the SnO$_2$:g-CN devices.

Time-resolved photoluminescence (TRPL) was used to examine the carrier lifetimes of the perovskite film. The fitted carrier lifetime is 418.32 ns for the SnO$_2$:g-CN sample, which is about 2.5 times as much as that of the control sample (169.06 ns), as shown in Figure 4d. According to the fitted trap-filled limited voltage (V_{TFL}) of the electron-only devices (Figure 4e), the electronic trap states were calculated to be 0.91×10^{16} and 1.53×10^{16} cm^{-3} for the SnO$_2$:g-CN and SnO$_2$ samples, respectively. Therefore, the superior carrier behavior and reduced trap states of the SnO$_2$:g-CN sample thanks to the enhanced film crystallization via buried manipulation. In addition, the enhanced storage stabilities in various environments of nonencapsulated SnO$_2$:g-CN devices are also validated (Figure 4f).

In summary, we have developed a new buried composite layer for optimizing vertical crystallization of the polycrystalline perovskites by introducing g-C$_3$N$_4$ nanosheets into the SnO$_2$ layer. We discover that the amine-rich g-C$_3$N$_4$ could not only improve the transmission, conductivity, and surface state of the buried transporting layer, contributing to the improved short-circuit current in devices, but also regulate the vertical qualities of the perovskite film, exhibiting superior carrier lifetimes with fewer trap states and thus enhanced device open-circuit voltage. Finally, the resultant devices realize a champion efficiency of 21.5% with all photovoltaic parameters enhanced. Our findings provide a new insight in manipulating the vertical nature of the polycrystalline perovskite films from the buried contact and a strategy to achieve efficient perovskite photovoltaic devices.

Supporting Information

Supporting Information is available from the Wiley Online Library or from the author.

Acknowledgements

Conflict of Interest

The authors declare no conflict of interest.

Data Availability Statement

Data available on request from the authors.

Keywords

[1] M. Jeong, I. W. Choi, E. M. Go, Y. Cho, M. Kim, B. Lee, S. Jeong, Y. Jo, H. W. Choi, J. Lee, J.-H. Bae, S. K. Kwak, D. S. Kim, C. Yang, *Science* **2020**, *369*, 1615.

[2] G. Kim, H. Min, K. S. Lee, D. Y. Lee, S. M. Yoon, S. I. Seok, *Science* **2020**, *370*, 108.

[3] D. Luo, W. Yang, Z. Wang, A. Sadhanala, Q. Hu, R. Su, R. Shivanna, G. F. Trindade, J. F. Watts, Z. Xu, T. Liu, K. Chen, F. Ye, P. Wu, L. Zhao, J. Wu, Y. Tu, Y. Zhang, X. Yang, W. Zhang, R. H. Friend, Q. Gong, H. J. Snaith, R. Zhu, *Science* **2018**, *360*, 1442.

[4] X. Zheng, Y. Hou, C. Bao, J. Yin, F. Yuan, Z. Huang, K. Song, J. Liu, J. Troughton, N. Gasparini, C. Zhou, Y. Lin, D.-J. Xue, B. Chen, A. K. Johnston, N. Wei, M. N. Hedhili, M. Wei, A. Y. Alsalloum, P. Maity, B. Turedi, C. Yang, D. Baran, T. D. Anthopoulos, Y. Han, Z.-H. Lu, O. F. Mohammed, F. Gao, E. H. Sargent, O. M. Bakr, *Nat. Energy* **2020**, *5*, 131.

[5] D. Luo, T. Zou, W. Yang, B. Xiang, X. Yang, Y. Wang, R. Su, L. Zhao, R. Zhu, H. Zhou, T. P. Russell, H. Yu, Z.-H. Lu, *Adv. Funct. Mater.* **2020**, *30*, 2001692.

[6] X. Yang, Y. Fu, R. Su, Y. Zheng, Y. Zhang, W. Yang, M. Yu, P. Chen, Y. Wang, J. Wu, D. Luo, Y. Tu, L. Zhao, Q. Gong, R. Zhu, *Adv. Mater.* **2020**, 2002585.

[7] Y. Tu, X. Yang, R. Su, D. Luo, Y. Cao, L. Zhao, T. Liu, W. Yang, Y. Zhang, Z. Xu, Q. Liu, J. Wu, Q. Gong, F. Mo, R. Zhu, *Adv. Mater.* **2018**, *30*, 1805085.

[8] Y. Tu, G. Xu, X. Yang, Y. Zhang, Z. Li, R. Su, D. Luo, W. Yang, Y. Miao, R. Cai, L. Jiang, X. Du, Y. Yang, Q. Liu, Y. Gao, S. Zhao, W. Huang, Q. Gong, R. Zhu, *Sci. China-Phys. Mech. Astron.* **2019**, *62*, 974221.

[9] D. Ouyang, Z. Huang, W. C. H. Choy, *Adv. Funct. Mater.* **2018**, 1804660.

[10] M. A. Haque, A. D. Sheikh, X. Guan, T. Wu, *Adv. Energy Mater.* **2017**, *7*, 1602803.

[11] Q. Jiang, X. Zhang, J. You, *Small* **2018**, 1801154.

[12] Q. Jiang, Z. Chu, P. Wang, X. Yang, H. Liu, Y. Wang, Z. Yin, J. Wu, X. Zhang, J. You, *Adv. Mater.* **2017**, *29*, 1703852.

[13] H. Lu, Y. Liu, P. Ahlawat, A. Mishra, W. R. Tress, F. T. Eickemeyer, Y. Yang, F. Fu, Z. Wang, C. E. Avalos, B. I. Carlsen, A. Agarwalla, X. Zhang, X. Li, Y. Zhan, S. M. Zakeeruddin, L. Emsley, U. Rothlisberger, L. Zheng, A. Hagfeldt, M. Grätzel, *Science* **2020**, *370*, 74.

[14] Q. Jiang, Y. Zhao, X. Zhang, X. Yang, Y. Chen, Z. Chu, Q. Ye, X. Li, Z. Yin, J. You, *Nat. Photonics* **2019**, *13*, 460.

[15] J. J. Yoo, G. Seo, M. R. Chua, T. G. Park, Y. Lu, F. Rotermund, Y.-K. Kim, C. S. Moon, N. J. Jeon, J.-P. Correa-Baena, V. Bulović, S. S. Shin, M. G. Bawendi, J. Seo, *Nature* **2021**, *590*, 587.

[16] E. H. Jung, B. Chen, K. Bertens, M. Vafaie, S. Teale, A. Proppe, Y. Hou, T. Zhu, C. Zheng, E. H. Sargent, *ACS Energy Lett.* **2020**, *5*, 2796.

[17] J. Wei, F. Guo, X. Wang, K. Xu, M. Lei, Y. Liang, Y. Zhao, D. Xu, *Adv. Mater.* **2018**, *30*, 1805153.

[18] J. Zhou, X. Wei, J. Zhu, X. Yang, H. Niu, L. Wan, P. Jiang, J. Xu, R. Zhou, G. Cao, *Sci. China Mater.* **2020**, *63*, 1151.

[19] F. Guo, X. Sun, B. Liu, Z. Yang, J. Wei, D. Xu, *Angew. Chem. Int. Ed.* **2019**, *58*, 18460.

[20] S. You, H. Zeng, Z. Ku, X. Wang, Z. Wang, Y. Rong, Y. Zhao, X. Zheng, L. Luo, L. Li, S. Zhang, M. Li, X. Gao, X. Li, *Adv. Mater.* **2020**, *32*, 2003990.

[21] K. Gkini, I. Martinaiou, P. Falaras, *Materials* **2021**, *14*, 1679.

[22] L.-L. Jiang, Z.-K. Wang, M. Li, C.-C. Zhang, Q.-Q. Ye, K.-H. Hu, D.-Z. Lu, P.-F. Fang, L.-S. Liao, *Adv. Funct. Mater.* **2018**, *28*, 1705875.

[23] J.-F. Liao, W.-Q. Wu, J.-X. Zhong, Y. Jiang, L. Wang, D.-B. Kuang, *J. Mater. Chem. A* **2019**, *7*, 9025.

[24] X. Wei, X. Liu, H. Liu, S. Yang, H. Zeng, F. Meng, X. Lei, J. Liu, *Sol. Energy* **2019**, *181*, 161.

[25] J. Chen, H. Dong, L. Zhang, J. Li, F. Jia, B. Jiao, J. Xu, X. Hou, J. Liu, Z. Wu, *J. Mater. Chem. A*, **2020**, *8*, 2644.

[26] P. Liu, Y. Sun, S. Wang, H. Zhang, Y. Gong, F. Li, Y. Shi, Y. Du, X. Li, S. Guo, Q. Tai, C. Wang, X.-Z. Zhao. *J. Power Sources* **2020**, *451*, 227825.

[27] L. Ge, C. Han, *Appl. Catal. B: Environ.* **2012**, *117*, 268.

[28] A. Thomas, A. Fischer, F. Goettmann, M. Antonietti, J.-O. Muller, R. Schlogl, J. M. Carlsson, *J. Mater. Chem.* **2008**, *18*, 4893.

[29] G. Gaggiotti, A. Galdikas, S. Kačiulis, G. Mattogno, A. Šetkus, *J. Appl. Phys.* **1994**, *76*, 4467.

[30] M. Jost, S. Albrecht, L. Kegelmann, C. M. Wolff, F. Lang, B. Lipovsek, J. Krc, L. Korte, D. Neher, B. Rech, M. Topic, *ACS Photonics* **2017**, *4*, 1232.

[31] X. Yang, J. Wu, T. Liu, R. Zhu, *Small Methods* **2018**, *2*, 1800110.

[32] K. Deng, Z. Liu, M. Wang, L. Li, *Adv. Funct. Mater.* **2019**, *29*, 1900830.

[33] X. Yang, D. Luo, Y. Xiang, L. Zhao, M. Anaya, Y. Shen, J. Wu, W. Yang, Y.-H. Chiang, Y. Tu, R. Su, Q. Hu, H. Yu, G. Shao, W. Huang, T. P. Russell, Q. Gong, S. D. Stranks, W. Zhang, R. Zhu, *Adv. Mater.* **2021**, *33*, 2006435.

[34] C. Bi, Q. Wang, Y. Shao, Y. Yuan, Z. Xiao, J. Huang, *Nat. Commun.* **2015**, *6*, 7747.

[35] X. Yang, Y. Ni, Y. Zhang, Y. Wang, W. Yang, D. Luo, Y. Tu, Q. Gong, H. Yu, R. Zhu, *ACS Energy Lett.* **2021**, *6*, 2404.

[36] G. Yang, C. Wang, H. Lei, X. Zheng, P. Qin, L. Xiong, X. Zhao, Y. Yan, G. Fang, *J. Mater. Chem. A* **2017**, *5*, 1658.

[37] W. Deng, X. Liang, P. S. Kubiak, P. J. Cameron, *Adv. Energy Mater.* **2018**, *8*, 1701544.